The Astrophysical Journal, 857:7 (15pp), 2018 April 10 https://doi.org/10.3847/1538-4357/aab4f4

The Orion Fingers: H_2 Temperatures and Excitation in an Explosive Outflow

Allison Youngblood[1,2,6], Kevin France[1,2,3], Adam Ginsburg[4], Keri Hoadley[5], and John Bally[2,3]
[1] Laboratory for Atmospheric and Space Physics, University of Colorado, 600 UCB, Boulder, CO 80309, USA; allison.a.youngblood@nasa.gov
[2] Department of Astrophysical and Planetary Sciences, University of Colorado, UCB 389, Boulder, CO 80309, USA
[3] Center for Astrophysics and Space Astronomy, University of Colorado, 389 UCB, Boulder, CO 80309, USA
[4] National Radio Astronomy Observatory, Socorro, NM 87801, USA
[5] Department of Astronomy, California Institute of Technology, 1200 East California Boulevard, Pasadena, CA 91125, USA
Received 2018 January 31; revised 2018 March 3; accepted 2018 March 5; published 2018 April 6

Abstract

We measure H_2 temperatures and column densities across the Orion Becklin-Neugebauer/Kleinmann-Low (BN/KL) explosive outflow from a set of 13 near-infrared (IR) H_2 rovibrational emission lines observed with the TripleSpec spectrograph on Apache Point Observatory's 3.5 m telescope. We find that most of the region is well characterized by a single temperature (∼2000–2500 K), which may be influenced by the limited range of upper-energy levels (6000–20,000 K) probed by our data set. The H_2 column density maps indicate that warm H_2 comprises 10^{-5}–10^{-3} of the total H_2 column density near the center of the outflow. Combining column density measurements for co-spatial H_2 and CO at $T = 2500$ K, we measure a CO/H_2 fractional abundance of 2×10^{-3} and discuss possible reasons why this value is in excess of the canonical 10^{-4} value, including dust attenuation, incorrect assumptions on co-spatiality of the H_2 and CO emission, and chemical processing in an extreme environment. We model the radiative transfer of H_2 in this region with ultraviolet (UV) pumping models to look for signatures of H_2 fluorescence from H I Lyα pumping. Dissociative (J-type) shocks and nebular emission from the foreground Orion H II region are considered as possible Lyα sources. From our radiative transfer models, we predict that signatures of Lyα pumping should be detectable in near-IR line ratios given a sufficiently strong source, but such a source is not present in the BN/KL outflow. The data are consistent with shocks as the H_2 heating source.

Key words: ISM: clouds – ISM: jets and outflows – stars: formation

Supporting material: data behind figures

1. Introduction

The Orion Becklin-Neugebauer/Kleinmann-Low (BN/KL) outflow is a ∼500 year-old explosion of dense gas emanating from the Orion Molecular Cloud (OMC1) core, which likely caused by the dynamical decay or merger of a multiple system of massive stars (Bally & Zinnecker 2005; Bally et al. 2017; Luhman et al. 2017). Over 100 well-collimated jet-like structures have been observed in infrared (IR) H_2 emission (termed "H_2 fingers"; Bally et al. 2015), and more continue to be found with high-resolution near-IR spectroscopy that can velocity-resolve H_2 fingers that are spatially coincident along our line of sight (Oh et al. 2016). The 3D structure of the dense gas as traced by CO in low-J (Zapata et al. 2009; Bally et al. 2017), mid-J (Peng et al. 2012), and high-J (Goicoechea et al. 2015) emission all indicate that CO appears to closely follow the inner H_2 fingers (Bally et al. 2017). The fingers' morphology and velocity vectors trace back to a common origin at approximately the same time, indicating that the outflow is due to a single explosive event that occurred ∼500 years ago. Kinematic studies of the embedded massive stars near the outflow origin have determined that three or four massive young stars were within several hundred au of each other at the time of the explosion (although it is uncertain which stars were coincident), indicating a dynamical interaction as the impetus (e.g., Tan 2004; Gómez et al. 2008; Plambeck et al. 2009; Goddi et al. 2011; Chatterjee & Tan 2012; Plambeck & Wright 2016; Dzib et al. 2017; Rodriguez et al. 2017).

Located just behind the Orion Nebula at a distance of 414 ± 7 pc (Menten et al. 2007), most of the BN/KL outflow is heavily reddened with visual extinctions ranging from 3–10 mag (Youngblood et al. 2016). The majority of the H_2 fingers associated with the BN/KL outflow can only be observed at longer wavelengths due to reddening. Some of the H_2 fingers (e.g., HH 201) are emerging from the dense OMC1 region into the foreground photo-dissociation region (PDR) and ionization front that separates the Orion blister H II region and OMC1, and they have been well studied at optical wavelengths (Doi et al. 2004). Because the H_2 fingers are bright, cover a large region of the sky (∼3′ × 3′), and have a curious origin, they have been extensively studied as a testbed for H_2 excitation mechanisms including shocks, UV fluorescence, and formation pumping (e.g., Beckwith et al. 1978; Snell et al. 1984; Rosenthal et al. 2000; Bally & Zinnecker 2005; Colgan et al. 2007; Zapata et al. 2009; Bally et al. 2011, 2015, 2017; Oh et al. 2016; Youngblood et al. 2016; Geballe et al. 2017). The consensus is that no single shock model can satisfactorily explain the H_2 observations; there appears to be a superposition of post-shock temperatures and C- and J-type shocks with varying magnetic field strengths. Thorough observational constraints are needed to drive the advancement of shock models.

The H_2 fingers are also important to study because dynamical interactions between massive stars in young star-forming regions are likely common, and the large amounts of energy released (∼10^{47} erg for BN/KL; Kwan & Scoville 1976;

[6] Now located at NASA Goddard Space Flight Center, Greenbelt, MD 20771, USA.

Table 1
Observed H_2 Emission Lines

Transition	$(v_u, J_u) \rightarrow (v_l, J_l)$	E_u (K)	λ_0 (Å)	A_{ul} (10^{-7} s^{-1})	Lyα Cascade[a] (%)
1–0 S(0)	(1, 2) → (0, 0)	6471	22235	2.53	4.0
1–0 S(1)	(1, 3) → (0, 1)	6951	21218	3.47	11.6
1–0 S(7)	(1, 9) → (0, 7)	12823	17480	2.98	0.08
1–0 S(8)	(1, 10) → (0, 8)	14233	17147	2.34	0.40
1–0 S(9)	(1, 11) → (0, 9)	15747	16877	1.68	0.001
2–1 S(0)	(2, 2) → (1, 0)	12095	23556	3.68	1.8
2–1 S(1)	(2, 3) → (1, 1)	12550	22477	4.98	7.4
3–2 S(3)	(3, 5) → (2, 3)	19086	22014	5.65	3.3
3–2 S(5)	(3, 7) → (2, 5)	20858	20656	4.53	0.27
1–0 Q(1)	(1, 1) → (0, 1)	6149	24066	4.29	9.1
1–0 Q(2)	(1, 2) → (0, 2)	6471	24134	3.03	4.7
1–0 Q(3)	(1, 3) → (0, 3)	6951	24237	2.78	9.3
1–0 Q(4)	(1, 4) → (0, 4)	7584	24375	2.65	6.3

Note. Upper-level energies (E_u) and wavelengths (λ_0) calculated via Herzberg (1950). Einstein A coefficients (A_{ul}) are from Wolniewicz et al. (1998).
[a] The Lyα cascade column denotes what percentage of the flux pumped from the (2, 5) and (2, 6) levels cascades through these lines. The ortho transitions' percentages are calculated by normalizing to the flux pumped out of (2, 5), and the para transitions' percentages are calculated by normalizing to the flux pumped out of the (2, 6) level of the ground electronic state. See Table 3 for a complete list of strong H_2 lines and the percentage of the Lyα cascade flux that appears in each line.

Snell et al. 1984) could be an important source of feedback in molecular clouds. Other possible BN/KL-like events include DR21 (Zapata et al. 2013), W49 Source G (Smith et al. 2009), G34.26 + 0.15 (Cyganowski et al. 2008), IRAS 05506 + 2414 (Sahai et al. 2008), and NGC 7129 (Eislöffel 2000; Gutermuth et al. 2004), all in the Milky Way Galaxy, and SPIRITS 14ajc in M83 (Kasliwal et al. 2017). However, these other systems are more distant (>1 kpc), making BN/KL the ideal prototype for detailed study of this potentially common phenomenon.

Many previous studies have analyzed the excitation mechanisms of the H_2 fingers by comparing the flux ratios of multiple H_2 transitions (e.g., Rosenthal et al. 2000; Colgan et al. 2007; Oh et al. 2016), although no set of observations have yet obtained full spatial coverage of the outflow with high-spatial resolution and high-spectral resolution. These past studies argue that throughout the outflow, the H_2 emission is characterized by warm temperatures (2000–3000 K), consistent with shock excitation, with evidence of small contributions from fluorescence from stellar, accretion, or nebular emission. Recently, a hot temperature component ($T \sim 5000$ K) comprising a few percent of the H_2 population has been observed in BN/KL, and is likely due to H_2 formation pumping (Geballe et al. 2017). H_2 formation occurs predominantly on dust grains, as gas-phase formation is slow. Some of the 4.5 eV H_2 binding energy is kept by the H_2 molecule after it is ejected from the dust grain, thus "pumping" it into excited (v, J) states and indicating temperatures larger than the molecular dissociation temperature ($T_{\rm dissoc} \sim 4500$ K). The presence of formation pumping indicates that the shocks are at least somewhat dissociative, and thus should emit high-energy radiation that could create a fluorescent H_2 population.

Non-thermal H_2 populations due to radiative excitation from Lyα photons (1215.67 Å) have been observed in planetary nebulae (Lupu et al. 2006), accreting T Tauri stars (Herczeg et al. 2002; Walter et al. 2003; France et al. 2012), reflection nebulae (Le et al. 2017), and several Herbig Haro objects (Schwartz 1983). The source of Lyα can either be nebular (H I recombination), from a central source (stellar or accretion), or intrinsic to the shock itself (H I recombination). In the recombination regions behind bow shocks, cooling is dominated by Lyman and Balmer H I transitions, producing strong Lyα emission. Lyα spectrally coincides with strong Lyman band H_2 transitions, but these transitions pump out of rotationally and/or vibrationally excited states ($E > 10{,}000$ K; typically $v \geqslant 2$). Thus, the H_2 population must be hot ($T \sim 2000$ K) to absorb Lyα photons.

Using the near-IR position–position–velocity (PPV) cube from Youngblood et al. (2016) with 1 square arcsecond spaxels and 86 km s^{-1} spectral resolution that covers the entire BN/KL outflow ($2\farcs7 \times 3\farcs3$), we determine the temperatures and column densities on a spaxel-by-spaxel basis from 13 observed H_2 emission lines. We also look for signatures of radiative excitation from nebular Lyα and intrinsic shock Lyα, which leave a non-thermal signature in the level populations of the ground electronic state.

Section 2 briefly describes the near-IR PPV cube and data products used for this analysis. Section 3 describes the temperatures and column densities determined across the outflow, and Section 4 compares the H_2 observations with previous CO observations, including a CO/H_2 abundance measurement for the hot gas. Section 5 discusses the signatures of non-thermal populations due to Lyα pumping, and Section 6 summarizes the results.

2. Near-IR H_2 Images

We utilize a near-IR (1.1–2.4 μm) position–position–velocity (PPV) cube of the Orion BN/KL outflow ($2\farcs7 \times 3\farcs3$) that was assembled from $R = 3500$ spectra from Apache Point Observatory's cross-dispersed TripleSpec spectrograph. The observations, data reduction, and the creation of derivative data products are described fully in Youngblood et al. (2016) and are available for public use.[7] The PPV cubes have a dispersion of 2.88 Å pix^{-1} and a spatial scale of $1''$ pix^{-1}. The derivative data products from the PPV cube include integrated intensity maps (observed and de-reddened) of 13 H_2 emission lines, a visual extinction map, radial velocity maps, and linewidth maps.

[7] The J, H, and K band PPV cubes are available for download at 10.7910/DVN/YUNZ1F.

We use the de-reddened integrated intensity maps of the 13 H_2 emission lines in this work (Table 1). Integrated intensities were measured by fitting Gaussians to the observed line profiles in the PPV cube and reddening was corrected for using the 1–0 Q(3) 24237 Å and 1–0 S(1) 21218 Å emission lines that originate from the same upper (v, J) state. The 13 lines vary significantly in signal-to-noise (S/N), thus each line has varying spatial coverage across the mapped region. The inner regions of the outflow are the brightest (Peaks 1 and 2; Beckwith et al. 1978) and have the most spectral line coverage.

Deep H_2 observations by Pike et al. (2016) and Geballe et al. (2017) have revealed that the 3–2 S(3) line (22014 Å) is significantly contaminated by the 4–3 S(5) line. The two lines are separated by 55 km s^{-1}, which is unresolved in the PPV cube (dispersion of 39 km s^{-1} pix^{-1} at 22014 Å), and the 4–3 S(5) line contributes ∼25% of the flux (Pike et al. 2016). We attempted to simultaneously fit one Gaussian for each line, but the fits were unsatisfactory. Thus, we have systematically decreased the flux in our 3–2 S(3) map by 25%.

For use in Section 5.3, we create a second visual extinction map based on the flux ratio between H I Brγ (21661 Å) and H I Paβ (12818 Å). Under Case B recombination at $T = 10^4$ K and $n_H = 10^4$ cm^{-3}, the intrinsic flux ratio $F(\mathrm{Br}\gamma)/F(\mathrm{Pa}\beta) = 0.17$ (Hummer & Storey 1987). We assume the near-IR extinction law from Mathis (1990). We compared this extinction map with that created from VLT/MUSE observations of Hα and Hβ (Weilbacher et al. 2015), and find them to agree within $A_V \sim 1$ mag.

3. Rovibrational Temperatures and Column Densities

We determine the H_2 temperatures on a spaxel-by-spaxel basis across the BN/KL outflow. Using the de-reddened intensities $I(v_u, J_u \rightarrow v_l, J_l)$ in erg cm^{-2} s^{-1} sr^{-1} of our 13 H_2 transitions, we calculate the H_2 column density in the upper states as

$$N(v_u, J_u) = \frac{4\pi\lambda_0}{hc}\frac{I(v_u, J_u \rightarrow v_l, J_l)}{A(v_u, J_u \rightarrow v_l, J_l)}, \quad (1)$$

where $A(v_u, J_u \rightarrow v_l, J_l)$ is the Einstein A coefficient from Wolniewicz et al. (1998). Equation (1) assumes that the H_2 emission is optically thin. Because the transition probabilities of the quadrupole transitions are small (∼10^{-7} s^{-1}; Table 1), the optical depth remains much less than unity until H_2 column densities approach 10^{24} cm^{-2}, which is orders of magnitude larger than the level column densities observed by previous authors for the BN/KL outflow, such as $N(v, J) \lesssim 10^{18}$ cm^{-2} from Rosenthal et al. (2000). However, we note that the measured column densities from Rosenthal et al. (2000) using the *Infrared Space Observatory* are potentially lower limits due to beam dilution.

We divide the level column densities $N(v_u, J_u)$ by their level degeneracy $g_{Ju} = g_s(2J_u+1)$, where $g_s = 3$ for ortho (odd J) H_2 and $g_s = 1$ for para (even J) H_2, and construct excitation diagrams by plotting the logarithm of $N(v_u, J_u)/g_{Ju}$ against the upper-level energy $E(v_u, J_u)/k_B$ (K). The upper-energy levels are calculated using equations and constants from Herzberg (1950). Temperatures and $(v, J) = (0, 0)$ column densities are derived from linear fits to the excitation diagrams, which is based on the Boltzmann equation:

$$\log_{10}\frac{N(v_u, J_u)}{g_{J_u}} = -\frac{1}{T \cdot \ln 10} \times \frac{E(v_u, J_u)}{k_B} + \log_{10} N(0, 0). \quad (2)$$

Total column density is recovered from $N(0, 0)$ by assuming a thermal distribution at the fitted temperature T. To compute a temperature via a linear fit for a given spaxel, we require at least three H_2 line fluxes from transitions originating from different upper-energy levels. Of the 21,270 $1'' \times 1''$ spaxels covered by the PPV cube, 11,246 spaxels contain at least three H_2 line fluxes, but only 9,302 spaxels contain three H_2 line fluxes from transitions that do not share an upper state.

In Figure 1, we present a temperature map based on fitting one temperature component, where we find that most temperatures are between 2000 and 3000 K. Figure 2 shows example temperature fits for marked spaxels in Figure 1, and Figure 3 shows the fractional temperature errors (σ_T/T) and the number of H_2 lines fitted. In the bright, central regions of the outflow (Peaks 1 and 2), the temperature errors are at their smallest: 3%–5%. Most of the temperatures have uncertainties <20%, and larger uncertainties typically correspond to fits with fewer available H_2 lines.

When using the observed H_2 intensities, rather than de-reddened values, calculated temperatures are underestimated. The higher E_u lines in the data set are at shorter wavelengths and are therefore more reddening sensitive. In the highest S/N regions of the PPV cube, the temperatures are underestimated by 100–400 K, which is significant when compared to the absolute temperature uncertainties in that region. Elsewhere, the temperature uncertainty is comparable to the difference between temperatures derived from observed and de-reddened intensities, meaning the reddening correction is not critically important in low-S/N data where other uncertainties dominate.

Some of the temperature fits in Figure 2 indicate the presence of H_2 populations that could be characterized by two temperatures. In many instances, the $J \leqslant 4$ lines in the $v = 1$ state (6000 K $< E_u <$ 8000 K) indicate cooler temperatures (steeper slopes) than found by the fits that include $E_u >$ 12,000 K lines. We create two additional temperature maps: one based on the six emission lines originating from the 6000 K $< E_u <$ 8000 K states, and one based on the seven emission lines originating from the 12,000 K $< E_u <$ 21,000 K states. The warm component contributes significantly to the cool component (Figure 2), so we extrapolate the warmer lines' fit to the upper-energy levels of the cooler lines and subtract the warm component. This leads to lower temperatures and higher column densities for the cool component than would be found without correcting for the warm component.

Using the cooler lines, we find significantly cooler temperatures across the outflow (∼1400 K; Figure 4). The morphology of this cooler temperature map is significantly different than the morphology of the temperature map in Figure 1 that uses lines from all of the states; it traces the 1–0 S(1) emission well. Because the cooler temperature component traces the H_2 fingers well, its excitation should be due to the shocks. Using the warmer lines, we find that the temperatures are on average 500 K warmer than the temperatures found using all the available lines. The morphology of this temperature map more

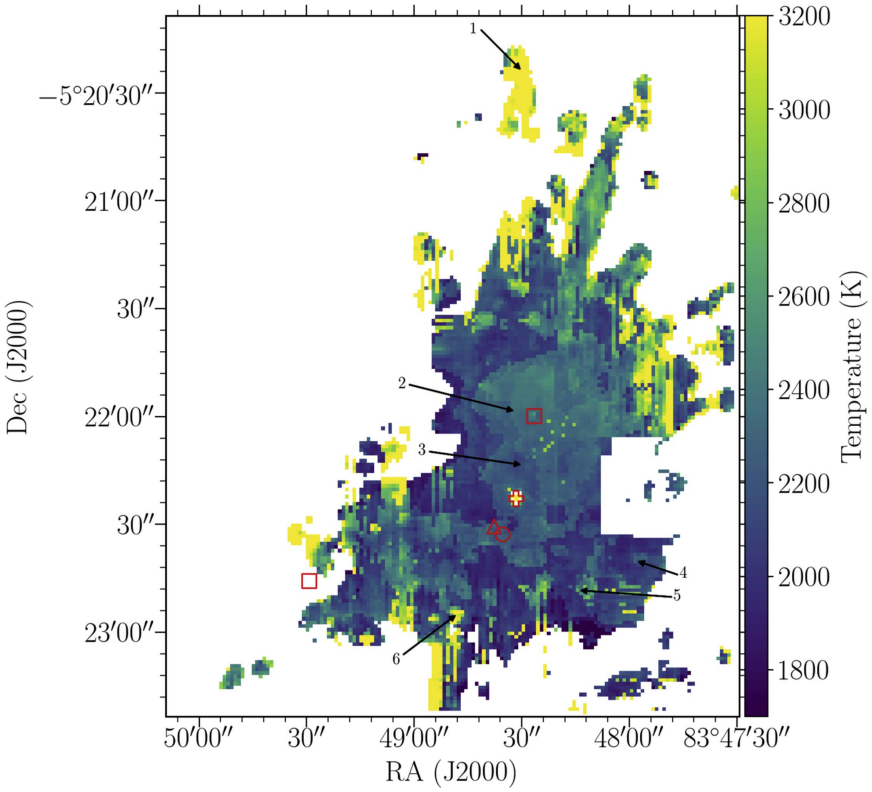

Figure 1. H_2 temperatures derived from the de-reddened H_2 intensities of all the available lines. The red plus sign, triangle, and open circle mark the locations of the BN object, source I, and source n, respectively. The red squares mark the locations of V2248 Ori (northwest) and MT Ori (southeast), continuum sources that contaminate some of the H_2 emission line maps. The labeled arrows show the spaxel locations of the sample fits shown in Figure 2. The data behind this figure is available as a FITS image. The data used to create this figure are available.

closely resembles the central, smooth temperature distribution of Figure 1, which is based off of all lines.

We consider, but discard, the possibility that this morphological smoothness of the warmer regions is due to scattering of the H_2 emission from regions heated by the region's embedded massive protostars. Burton et al. (1991) found a H_2 reflection nebula spatially coincident with Peaks 1 and 2, but concluded that the observed dichroic polarization is due to absorption from a foreground layer of aligned dust grains. Sugai et al. (1994) confirm that the polarized H_2 emission seen in Peaks 1 and 2 is intrinsic to the area and is polarized by foreground dust grains as opposed to being scattered into the line of sight.

From the excitation diagrams, we also measure the total column density of the H_2 population at the best-fit temperatures, which we refer to as $N(H_2, \text{hot})$ to distinguish it from the total column density of H_2 at all temperatures (Figure 5). For the fits using all 13 H_2 lines, $N(H_2, \text{hot})$ values range from approximately 10^{17}–10^{19} cm^{-2}, and larger columns trace the H_2 finger structure toward the center of the outflow. Larger $N(H_2, \text{hot})$ values are found when fitting only the $E_u < 8000$ K lines, and these values range from 10^{19}—10^{21}. This indicates that cooler gas dominates the H_2 population. The $N(H_2, \text{hot})$ values found when fitting only the $E_u > 12{,}000$ K lines are only slightly smaller than the values found from fitting all 13 lines. Using the dust extinction map from (Youngblood et al. 2016) and the dust-to-gas ratio from (Diplas & Savage 1994),we measure the total foreground H_2 column density at all temperatures to be $\sim 10^{22}$ cm^{-2}. Therefore, the rovibrationally excited or hot H_2 comprises 10^{-5}–10^{-3} of the total foreground H_2 column density.

3.1. Potential Biases and Systematic Errors

The set of 13 H_2 lines do not sample an upper-energy level range suitable to detect multiple temperature components. In Figure 6, we show two examples of realistic multi-temperature thermal populations, where a single temperature fits well, as indicated by the reduced chi-square values. Pike et al. (2016) also noted for K band observations the necessity of a two-temperature fit is not obvious unless lines from levels $E_u \geqslant 30{,}000$ K are included, or lines from levels $E_u < 6000$ K (Rosenthal et al. 2000).

The fitted temperatures are likely biased by which of the 13 lines are available to fit and the S/N of each of those lines. Figure 7 demonstrates that the goodness-of-fit metric χ^2_ν is correlated with the fitted temperature (Pearson correlation coefficient $\rho = 0.91$ and the probability of no correlation $n = 3 \times 10^{-8}$). The median fitted temperatures rise by approximately 100 K between fits using five H_2 lines and fits using all thirteen H_2 lines. Also, temperature fits with small numbers of H_2 lines ($\leqslant 7$) and large numbers of H_2 lines ($\geqslant 11$) have the best fits as defined by the χ^2_ν value. This is likely because of our two distinct populations of H_2 lines. Six of our lines originate from $E_u < 8000$ K and seven from $E_u > 12{,}000$ K, leaving a wide gap in probed energy levels, and the latter lines are lower S/N. It is apparent that fitting more lines reduces the χ^2_ν value. Fitting seven or fewer lines also reduces the χ^2_ν value, because for spaxels with seven or fewer lines measured, the available lines tend to come from the $E_u < 8000$ K population, which has higher S/N. It is possible that the fits to only the $E_u < 8000$ K lines are more consistent

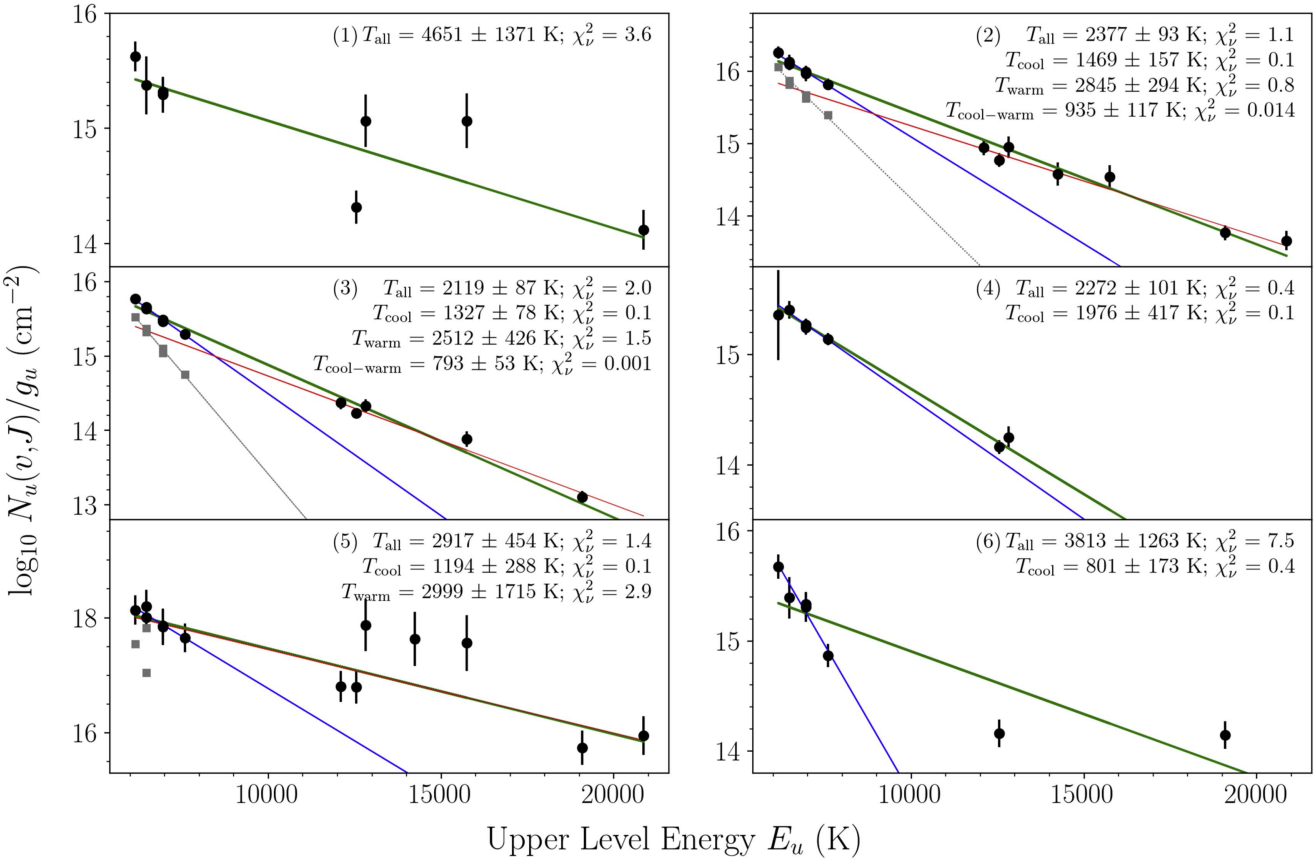

Figure 2. Representative H_2 temperature fits from six different $1'' \times 1''$ spaxels of the PPV cube. The numbers in parentheses correspond to the marked spaxels in Figure 1 and subsequent figures. The black points with error bars show the data, the green line shows the fits to all available H_2 lines ("all"), the blue line shows the fits to lines with $E_u < 8000$ K ("cool"), and the red line shows the fits to lines with $E_u > 12{,}000$ K ("warm"). The gray squares show the data for the "cool" upper levels after the "warm" component's contribution to those levels has been subtracted ("cool-warm"), and the gray dotted line shows the fit to the squares. Their error bars are large due to the uncertainty in the subtracted "warm" fit and are not shown for visual clarity. The best-fit temperature, uncertainty, and reduced chi-square value for each case is printed at the top of each diagram.

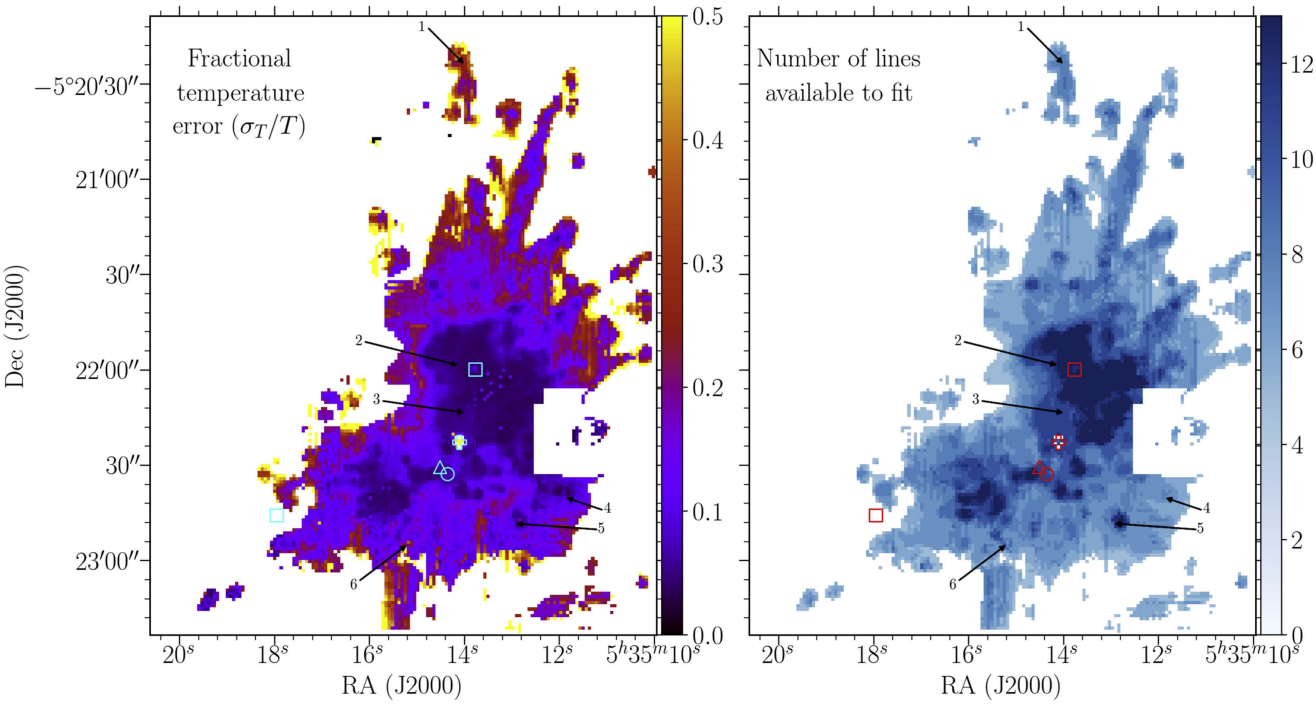

Figure 3. Left: the fractional uncertainty in the H_2 temperature, σ_T divided by the temperature T. Right: the number of H_2 emission lines used in the temperature fit for each spaxel. The minimum is three, and the maximum is 13.

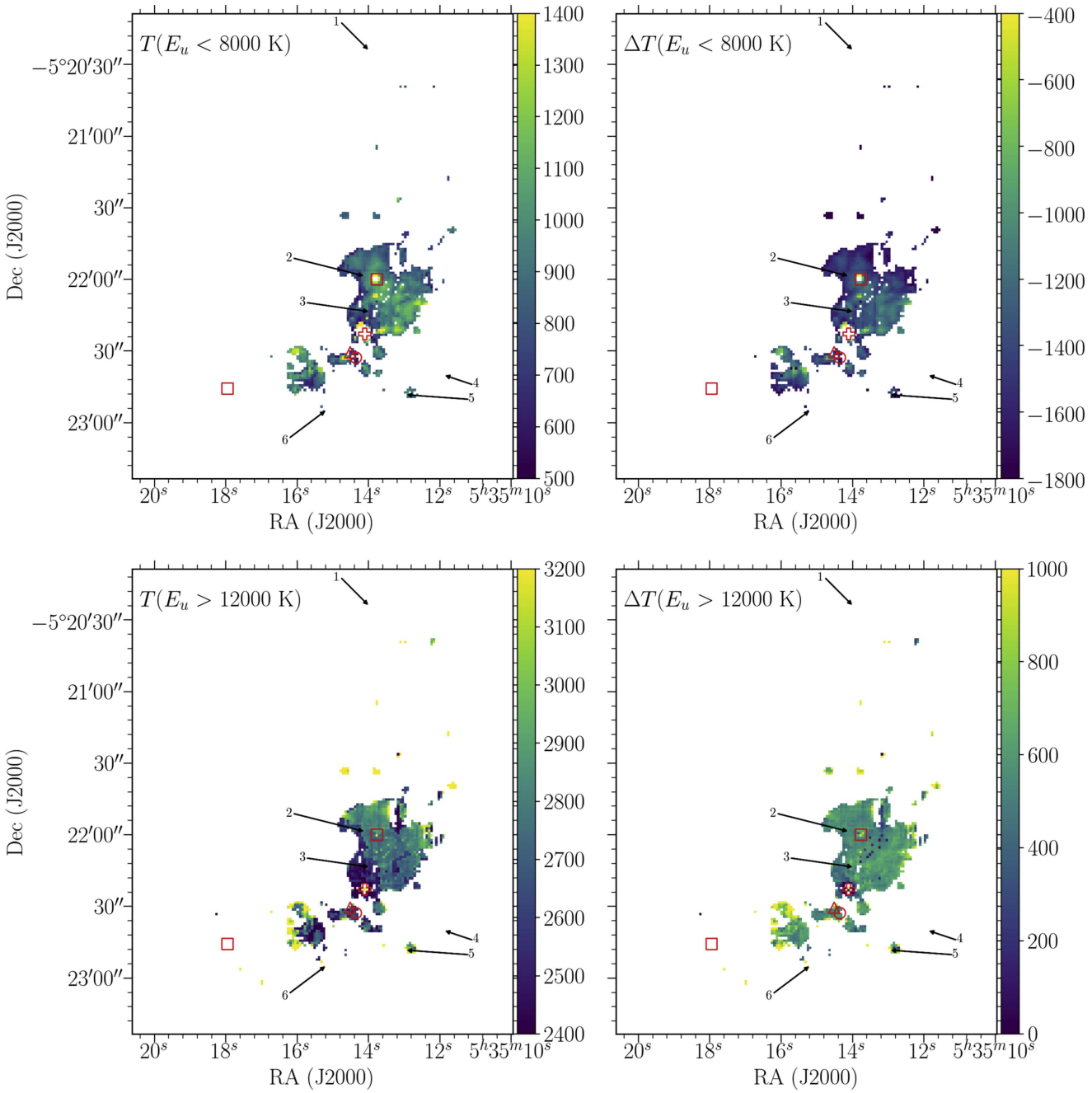

Figure 4. Top Left: the temperature (K) derived using only the H_2 emission lines that originate from upper levels with $E_u < 8000$ K after the fit to the $E_u > 12{,}000$ K lines has been subtracted. Top right: the cooler $E_u < 8000$ K temperatures with the hotter "average" temperature (derived using all of the observed lines; Figure 1) subtracted. The color bar shows the difference in the two temperature maps in Kelvin. Bottom left: the temperature (K) derived using only the $E_u > 12{,}000$ K lines. Bottom right: the warmer $E_u > 12{,}000$ K temperatures with the cooler "average" temperature subtracted.

with a single temperature than the fits that included the higher E_u lines as well, but as shown in Figure 6, this is likely not the case.

We also observe an increase in temperature with increasing distance from the center of the outflow, which coincides with the position of Source I within a few arcseconds (Figure 7). This temperature increase could be caused by faster shocks and/or lower volume density. Assuming a momentum-conserving explosion into a stationary medium, individual knots of ejected material become sorted by mass; the less massive knots attain higher velocities and travel farther from the origin. Higher outflow velocities will shock the gas to higher temperatures, potentially dissociating H_2 and leading to formation pumping and fluorescent excitation from radiative shocks. Also, the volume density n of the gas is expected to be less in the outer fingers according to the momentum-conserving explosion scenario. This implies that the cooling time of the gas, which is inversely proportional to n^2, is longer in the outer fingers and could explain the higher temperatures.

Thus, our relative temperature measurements are most robust in the central region of the outflow where there are more high-S/N lines available for fitting. Our absolute fitted temperatures

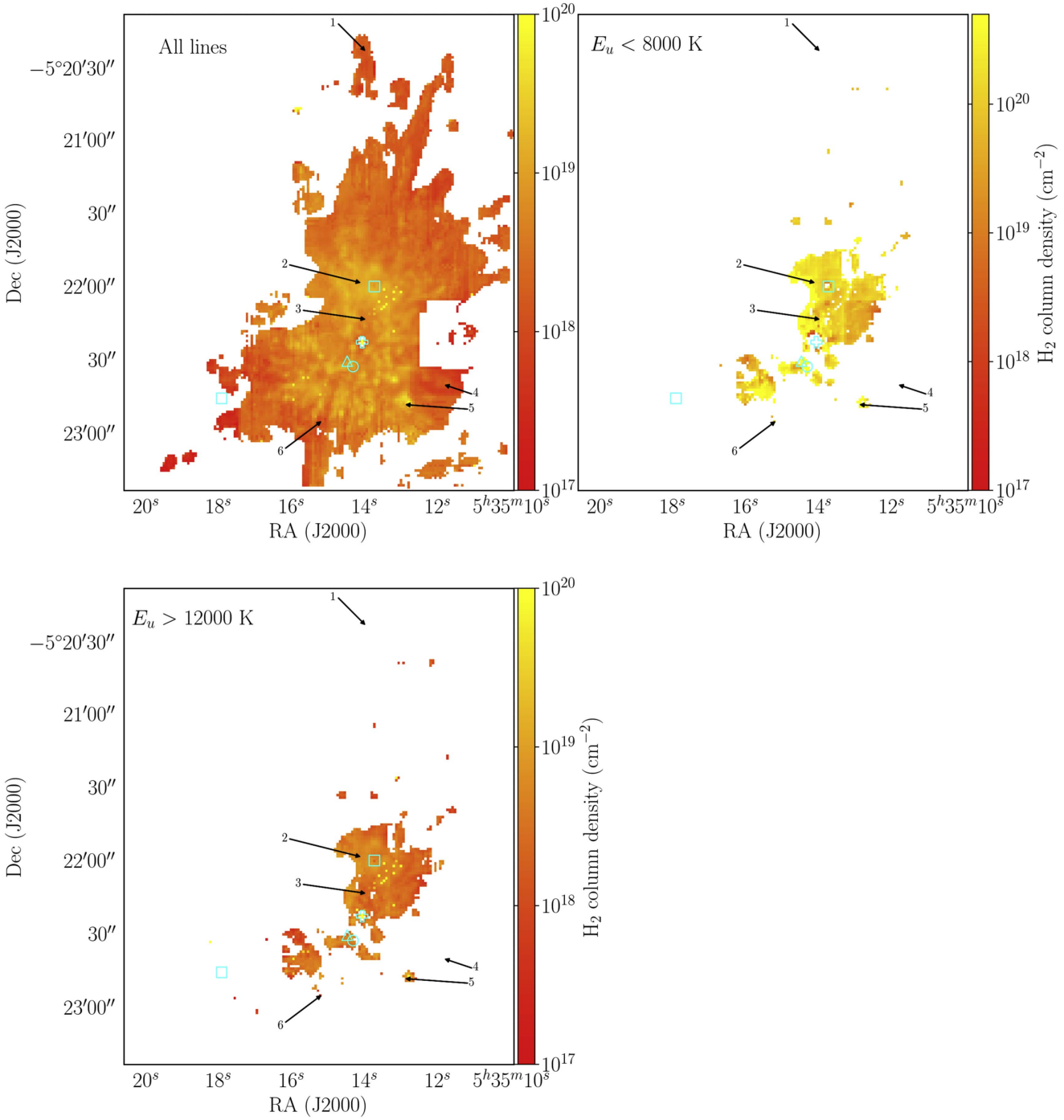

Figure 5. Total H_2 column density maps that correspond to the three temperature maps. Each spaxel's value represents the column density of H_2 at that spaxel's temperature. Top left: derived from fits to all 13 H_2 lines. Top right: derived from fits to the $E_u < 8000$ K lines after the fit to the $E_u > 12{,}000$ K lines has been subtracted. Bottom left: derived from fits to only the $E_u > 12{,}000$ K lines. The data behind this figure is available as a FITS image. The data used to create this figure are available.

are influenced by the available selection of H_2 lines and their upper-level energies ($6000 < E_u < 21{,}000$), and they typically have larger errors in the outer regions of the outflow.

4. Comparison with CO Observations

We compare our H_2 temperature ($T(H_2) \sim 2000$–3000 K) and column density measurements ($N(H_2) \sim 10^{17}$–10^{19} cm^{-2}) with ALMA and *Herschel* CO observations from the literature. Bally et al. (2017) mapped the entire BN/KL outflow in ^{12}CO $J = 2$–1 in high-spatial (1″–2″) and velocity resolution (1.3 km s^{-1}). This emission traces cold CO gas ($T_{\rm cold} =$ 20–90 K) at column densities similar to H_2, but the CO column densities are underestimated due to spatial filtering of the interferometer. ALMA confirmed Submillimeter Array observations that showed that these CO "streamers" are highly collimated and spatially coincident with the H_2 fingers, but only out to ∼1′ (Zapata et al. 2009). Beyond ∼1′, the H_2 fingers exhibit large velocities ($v > 100$ km s^{-1}) where shocks could completely dissociate the CO molecules.

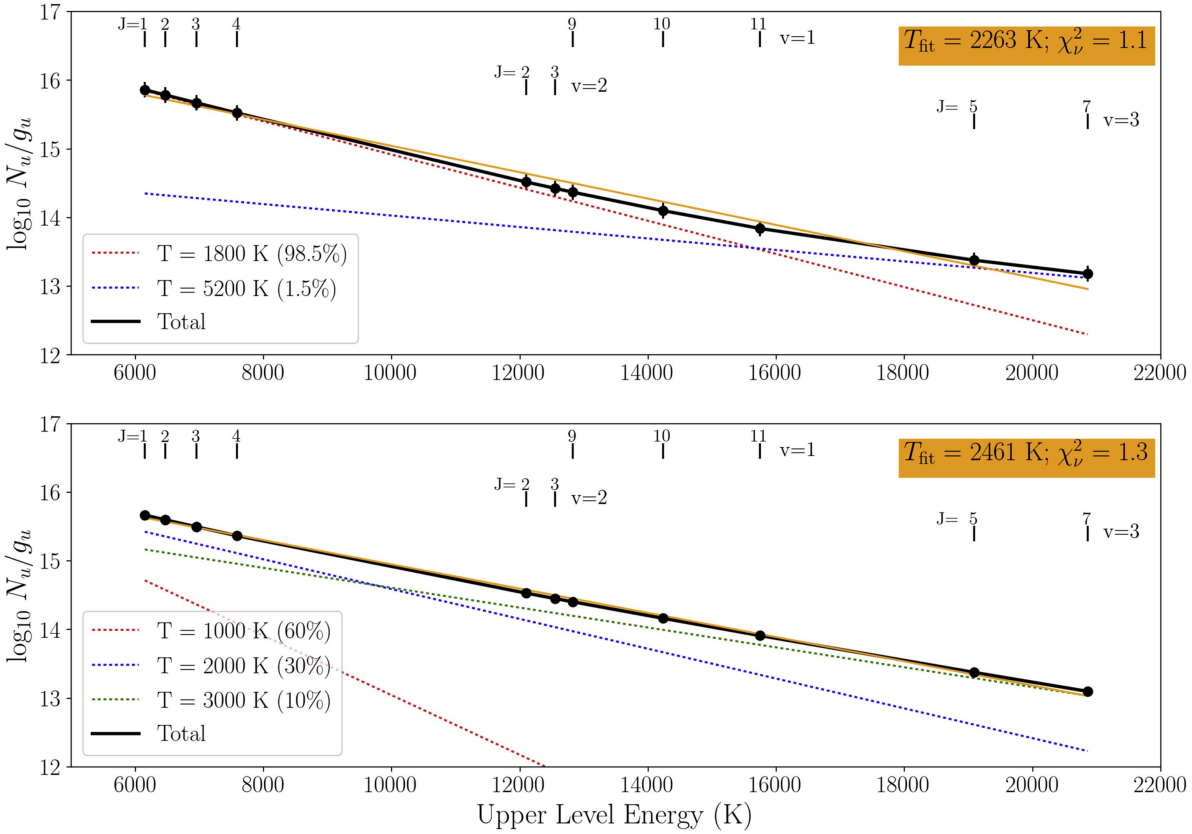

Figure 6. Example excitation diagrams of multi-temperature H_2 populations using our 13 near-IR H_2 lines. For both panels, the total H_2 column density was set to $\log_{10} N(H_2) = 19$ and ortho/para = 3. Top: 98.5% of the H_2 population is described by $T = 1800$ K (red dashed line), and 1.5% is described by $T = 5200$ K (blue dashed line) as Geballe et al. (2017) found for part of the BN/KL outflow. The orange line shows a single-temperature fit to the 13 points: $T = 2263$ K and $N(H_2) = 5.5 \times 10^{18}$ cm^{-2} with $\chi^2_\nu = 1.1$, indicating a good fit. Bottom: 60% of the H_2 population has $T = 1000$ K, 30% has $T = 2000$ K, and 10% has $T = 3000$ K. The orange line shows a single-temperature fit to the 13 points: $T = 2461$ K and $N(H_2) = 3.5 \times 10^{18}$ cm^{-2} with $\chi^2_\nu = 1.3$, indicating a good fit.

Alternatively, the dense clumps needed to drive these high-velocity shocks (Bally et al. 2015) are not as massive as the inner clumps and could be below the detection threshold ($T_{\rm brightness} < 0.1$ K). A momentum-conserving explosion like BN/KL will ensure that the lowest mass ejecta have the highest velocities, and are therefore the farthest from the explosion origin.

On the other hand, Goicoechea et al. (2015) mapped the inner $2' \times 2'$ BN/KL outflow in ^{12}CO up to $J = 48$–47 at $12''$ spatial resolution with *Herschel*. They found that multiple temperature components were required to explain the observations, with the hottest temperature component having a similar kinetic temperature to the near-IR H_2 gas ($T_{\rm hot} = 2500$ K). The near-IR H_2 and the hot CO observed by *Herschel* have a similar temperature and morphology, making it likely that they are co-spatial parcels of gas (Goicoechea et al. 2015).

We measure the CO/H_2 ratio of Peak 1 (the northwestern peak of H_2 intensity as seen at low spatial resolution; Beckwith et al. 1978) from the H_2 column densities measured in this work and the CO column density from *Herschel*. For the 2500 K CO component, Goicoechea et al. (2015) measured N(CO, hot) $= 1.5 \times 10^{16}$ cm^{-2} over a $30'' \times 30''$ box centered at α_{2000}: 5$^{\rm h}$35$^{\rm m}$13$^{\rm s}$.6, δ_{2000}: −5°22′07.″9. For this same region, we measure a mean value of $N(H_2,$ hot$) = 7.3 \times 10^{18}$ cm^{-2} after excluding the BN object (a known continuum contaminant in our emission line maps; Youngblood et al. 2016) and convolving the column density map derived from all H_2 lines to match the *Herschel* spatial resolution. This results in CO/$H_2 = 2 \times 10^{-3}$, and we estimate the uncertainty to be a factor of two.

Our measured CO/$H_2 = 2 \times 10^{-3}$ is an order of magnitude larger than those reported for cold, dense clouds (2×10^{-4}; Dickman 1978; Lacy et al. 1994, 2017), and even larger than the value for diffuse and translucent clouds (Burgh et al. 2007). Previously, authors made CO/H_2 measurements of Peak 1 and the surrounding area, but for colder gas. Wilson et al. (1986) found 5×10^{-5} for ∼100 K gas, and Watson et al. (1985) found 1.2×10^{-4} for 750 K gas. Models are in agreement with $10^{-7} \lesssim$ CO/$H_2 \lesssim 10^{-4}$ (van Dishoeck & Black 1988; Visser et al. 2009), but the majority of the temperature parameter space probed by models is considerably colder than 2500 K. In models of protoplanetary disks in transition, Bruderer (2013) finds some regions of parameter space (e.g., disks with small gas fractions) where CO/$H_2 > 10^{-3}$.

We consider the possibility that dust is hiding significant amounts of hot H_2 and thus raising the CO/H_2 ratio. Goicoechea et al. (2015) measured CO column density from $\lambda \sim 100\ \mu$m, while this work is centered around $\lambda = 2\ \mu$m. Assuming a standard extinction law from Mathis (1990), and that CO is unaffected by dust extinction, we find that $A_V = 17$ mag would be required to increase the typical CO/$H_2 = 2.7 \times 10^{-4}$ (Lacy et al. 1994) to 2×10^{-3} (this work). Using the Diplas & Savage (1994) relation between A_V and N(H) and assuming N(H) $\sim 2N(H_2)$, $A_V = 17$ mag corresponds to $N(H_2) = 7.5 \times 10^{21}$ cm^{-2}. Assuming a gas volume density of $n(H_2) = 10^6$ cm^{-3} (Bally et al. 2017) and spherical

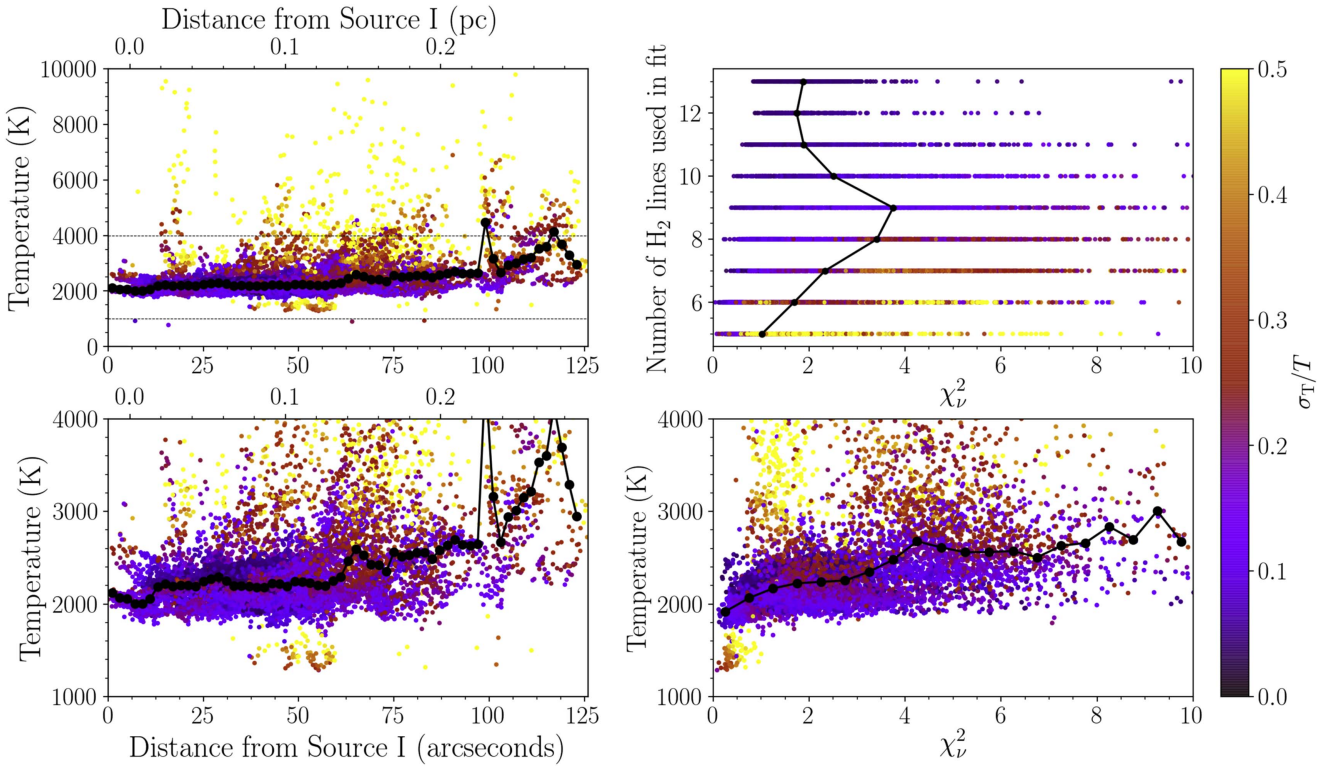

Figure 7. Top left: fitted temperature compared with the distance from Source I in arcseconds (bottom axis) and pc (top axis), assuming a distance of 414 pc. The dashed lines shows the temperature range corresponding to the bottom left plot. Each circle represents a spaxel and is color coded by the fractional uncertainty in the fitted temperature (σ_T/T). The black points represent the median values in each distance bin. Bottom left: similar to the top left plot, but shows a narrower temperature range as indicated by the dashed lines in the top left plot. Top right: the reduced chi-square (χ^2_ν) of the fit is shown against the number of H_2 lines used in the fit. Bottom right: the fitted temperature is shown against χ^2_ν.

symmetry, a cloud of diameter 0.003 pc or 500 au (1.″5 in projection at 414 pc) would result in $A_V = 17$ mag. In this scenario, $A_V = 17$ mag of extincting material lies behind the observed hot H_2 with $A_V \sim 5$ mag in front of the observed H_2. This implies that about 90% of the total hot H_2 and CO is behind the observed H_2 fingers. Other possible influences on our measured CO/H_2 ratio could be confused spatial stratification resulting from the large apertures of our measurements (e.g., France et al. 2014), and uncertainties in the CO column density derived from the *Herschel* data. Bruderer et al. (2012) discuss how uncertainty in H_2 formation rates at high gas temperatures can affect modeled high-J CO line intensities by a factor of a few, and therefore influence the derived column densities.

5. Non-thermal Populations

In Section 3, we have shown that the BN/KL outflow appears to be well characterized by a thermal distribution. The high velocities (>40 km s^{-1}) of the H_2 fingers and the presence of [Fe II] emission (Bally et al. 2015; Youngblood et al. 2016) indicate that many of these shocks are likely dissociative, have high post-shock temperatures, and therefore emit UV radiation (Wolfire & Konigl 1991). UV continuum or emission line flux can create non-thermal populations via fluorescence. To better characterize the excitation conditions of the BN/KL outflow, we consider in this section signatures of H_2 fluorescence created specifically by H I Lyα pumping (see Shull 1978 for an overview).

5.1. General Lyα Pumping and Radiative Cascade

First, we outline the general process of Lyα pumping and the resulting radiative cascade, and consider three test scenarios to find where the best signatures of Lyα pumping exist. Similar radiative transfer models of Lyα pumping of H_2 have been performed for protoplanetary disk and T Tauri stars showing signatures of H_2 absorption within observed Lyα wings extending several hundred km s^{-1} (Herczeg et al. 2004; Schindhelm et al. 2012; Hoadley et al. 2017).

A $\leqslant$200 km s^{-1} wide Lyα profile coincides spectrally with two strong Lyman band H_2 transitions. 1–2 R(6) (1215.73 Å) and 1–2 P(5) (1216.07 Å) pump H_2 molecules from the ground electronic state $X\ ^1\Sigma_g^+$ (v_l, J_l) = (2, 6), (2, 5), respectively, into the first excited electronic state $B\ ^1\Sigma_u^+$ (v_u, J_u) = (1, 7), (1, 4), respectively. The lifetimes of the (1, 7) and (1, 4) states are short ($\sim 10^{-8}$ s; Abgrall et al. 1993), and they decay back to an array of (v_l, J_l) levels in the ground electronic state following the dipole selection rules (Δv = any, $\Delta J = \pm 1$). We refer to these as the (1, 7) and (1, 4) progressions, and the strongest of these transitions ($A_{ul} > 5 \times 10^7$ s^{-1}) are listed in Table 2. Once back in the ground state, the (1, 7) and (1, 4) progressions cascade independently down to (v_l, J_l) = (0, 0) and (0, 1), respectively, following quadrupole selection rules (Δv = any, $\Delta J = 0, \pm 2$, $J = 0 \rightarrow 0$ forbidden). We treat the para and ortho states as independent species.

We calculate the Lyα flux pumped in the 1–2 R(6) and 1–2 P(5) lines using a procedure described in detail in McJunkin et al. (2016). We calculate the optical depths (τ_λ) of the Lyman band lines from absorption cross-sections (σ_{lu}) and column densities in the lower states $N(v_l, J_l)$. We then correct the

Table 2
Electronic H_2 Transitions: the (1, 4) and (1, 7) Progressions with $A_{ul} > 10^7$ s^{-1}

Transition	$(v_u, J_u) \rightarrow (v_l, J_l)$	λ_0 (Å)	A_{ul} (10^7 s^{-1})	Transition	$(v_u, J_u) \rightarrow (v_l, J_l)$	λ_0 (Å)	A_{ul} (10^7 s^{-1})
1–1 R(3)	(1, 4) → (1, 3)	1148.70	6.70	1–1 R(6)	(1, 7) → (1, 6)	1161.95	6.35
1–1 P(5)	(1, 4) → (1, 5)	1161.82	8.47	1–1 P(8)	(1, 7) → (1, 8)	1183.31	7.53
1–2 R(3)	(1, 4) → (2, 3)	1202.45	13.38	1–2 R(6)[a]	(1, 7) → (2, 6)	1215.73	13.62
1–2 P(5)*	(1, 4) → (2, 5)	1216.07	15.92	1–2 P(8)	(1, 7) → (2, 8)	1237.87	14.69
1–3 R(3)	(1, 4) → (3, 3)	1257.83	11.92	1–3 R(6)	(1, 7) → (3, 6)	1271.02	13.42
1–3 P(5)	(1, 4) → (3, 5)	1271.93	12.76	1–3 P(8)	(1, 7) → (3, 8)	1293.87	12.27
1–6 R(3)	(1, 4) → (6, 3)	1431.01	9.98	1–6 R(6)	(1, 7) → (6, 6)	1442.87	9.32
1–6 P(5)	(1, 4) → (6, 5)	1446.12	14.19	1–6 P(8)	(1, 7) → (6, 8)	1467.08	13.46
1–7 R(3)	(1, 4) → (7, 3)	1489.57	16.24	1–7 R(6)	(1, 7) → (7, 6)	1500.45	16.97
1–7 P(5)	(1, 4) → (7, 5)	1504.76	19.76	1–7 P(8)	(1, 7) → (7, 8)	1524.65	18.70
1–8 R(3)	(1, 4) → (8, 3)	1547.34	11.48	1–8 R(6)	(1, 7) → (8, 6)	1556.87	12.50
1–8 P(5)	(1, 4) → (8, 5)	1562.39	12.27	1–8 P(8)	(1, 7) → (8, 8)	1580.67	10.99

Note. All transitions are between $B\ ^1\Sigma_u^+$ and $X\ ^1\Sigma_g^+$. Wavelengths and Einstein A coefficients are from Abgrall et al. (1993).
[a] 1–2 P(5) and 1–2 R(6) are the transitions pumped by Lyα.

optical depths as described in Liu & Dalgarno (1996) and Wolven et al. (1997), because the wings of the two absorbing lines overlap. We attenuate the assumed intrinsic Lyα profile using the corrected optical depths and integrate over the absorbed flux to calculate the pumping flux. The pumping fluxes are put directly into the (1, 7) and (1, 4) states of the first excited electronic state, where they are promptly redistributed via branching ratios ($r_{branch} = A_{ul}/\sum A_{ul}$; Table 2) back into the ground electronic state. The probability of dissociation from the (1, 7) and (1, 4) upper levels is zero (Abgrall et al. 2000; Herczeg et al. 2006).

We then compute the flux in each rovibrational ground state transition as the H_2 molecules cascade down, following the quadrupole selection rules of the ground electronic state ($\Delta v =$ any, $\Delta J = 0, \pm 2$, $J = 0 \rightarrow 0$ forbidden). The cascade is computed using branching ratios calculated from the Einstein A coefficients from Wolniewicz et al. (1998). We consider the cascade fluxes as an "excess" compared to the fluxes determined from a thermally populated ground state in equilibrium. Because the lifetimes of these ground state levels are long ($\sim 10^7$ s; Wolniewicz et al. 1998), we assume that each cascading molecule that reaches $(v_l, J_l) = (2, 6)$ or (2, 5) is re-pumped immediately by Lyα into the (1, 7) and (1, 4) levels in the excited state. Effectively, the cascade ends when reaching the (2, 6) or (2, 5) levels, where it is re-pumped into (1, 7) and (1, 4). This re-pumped flux is 15.3% of the initial pumping flux for the (1, 7) progression and 2.5% for the (1, 4) progression. Allowing multiple pumpings creates a small effect on the resulting excitation diagrams as the fitted temperatures are changed by $\leqslant$100 K and the column densities are changed by $\leqslant$0.1 dex. We find that more than three multiple pumpings causes negligible additional modification of the H_2 populations, and we truncated the multiple pumping chain at three.

Figure 8 shows an example of the excess flux in our 13 H_2 lines produced by the radiative cascade following Lyα pumping. We consider three limiting cases where (a) the Lyα flux pumped into (1, 7) and (1, 4) are equal, (b) flux was pumped into (1, 7) but not (1, 4), and (c) flux was pumped into (1, 4) but not (1, 7). 0.05 erg cm^{-2} s^{-1} sr^{-1} was chosen as an example value that would have a large effect on the excitation diagram. Of our 13 near-IR H_2 lines (Table 1), we find that all but 1–0 S(7), 1–0 S(8), and 1–0 S(9) should show excess flux due to Lyα pumping if both the (2, 6) and (2, 5) states are pumped. We also consider other near-IR and mid-IR H_2 lines, many of which have been detected in Orion BN/KL by other instruments (Rosenthal et al. 2000; Oh et al. 2016; Geballe et al. 2017) or are expected to be detected. The lines that show the largest increases are the 0–0 S-branch lines in the mid-IR from 8–28.2 μm. However, excess flux in low (v, J) emission lines will be greatly diminished by collisional de-excitation, which is discussed more in Section 5.4. In Table 3, we present a list of H_2 transitions through which $\geqslant$0.1% of the pumping Lyα flux passes during the radiative cascade. In general, lines originating from $J_u \gtrsim 10$ receive negligible Lyα flux.

5.2. Intrinsic Lyα from the Post-shock Region

We assume a Lyα profile that originates from the H_2 fingers themselves. Fast, dissociative shocks (J-type shocks) emit UV radiation, including Lyα that has been observed to pump rovibrationally excited H_2 populations (e.g., Wolfire & Konigl 1991). Walter et al. (2003) found evidence of this in the outflow from T Tauri; the Lyα radiation is described by a profile that is narrow compared to the broad (several hundred km s^{-1}) Lyα emission from the accreting star. Walter et al. (2003) do not place a direct constraint on the line shape, but find that only the 1–2 R(6) and 1–2 P(5) Lyman band H_2 transitions are responsible for the observed fluorescence in the outflow. The velocity separation of these two transitions, 1–2 R(6) at 1215.73 Å and 1–2 P(5) at 1216.07 Å, indicates that the Lyα line must have significant flux over 0.34 Å (84 km s^{-1}), as measured at the base of the line.

We assume a narrow (40 km s^{-1}) and a broad (100 km s^{-1}) profile. From the shock models of Hartigan et al. (1987), we estimate the Lyα integrated flux through the front of the shock to be approximately 10^{-3} erg cm^{-2} s^{-1} sr^{-1} for a variety of shock velocities. This model surface brightness is in agreement with a simple calculation that assumes every H atom passing through the shock is ionized, then recombines. 68% of recombinations under Case B assumptions (optically thick in all Lyman lines) result in a Lyα photon, so the Lyα photon surface brightness through the shock is $1/(4\pi) \cdot 0.68 \cdot n_{\text{pre-shock}} \cdot V_{\text{shock}}$, where $n_{\text{pre-shock}}$ is the pre-shock hydrogen density, and V_{shock} is the shock velocity. Assuming $n_{\text{pre-shock}} = 100$ cm^{-2} and $V_{\text{shock}} = 100$ km s^{-1} (typical values

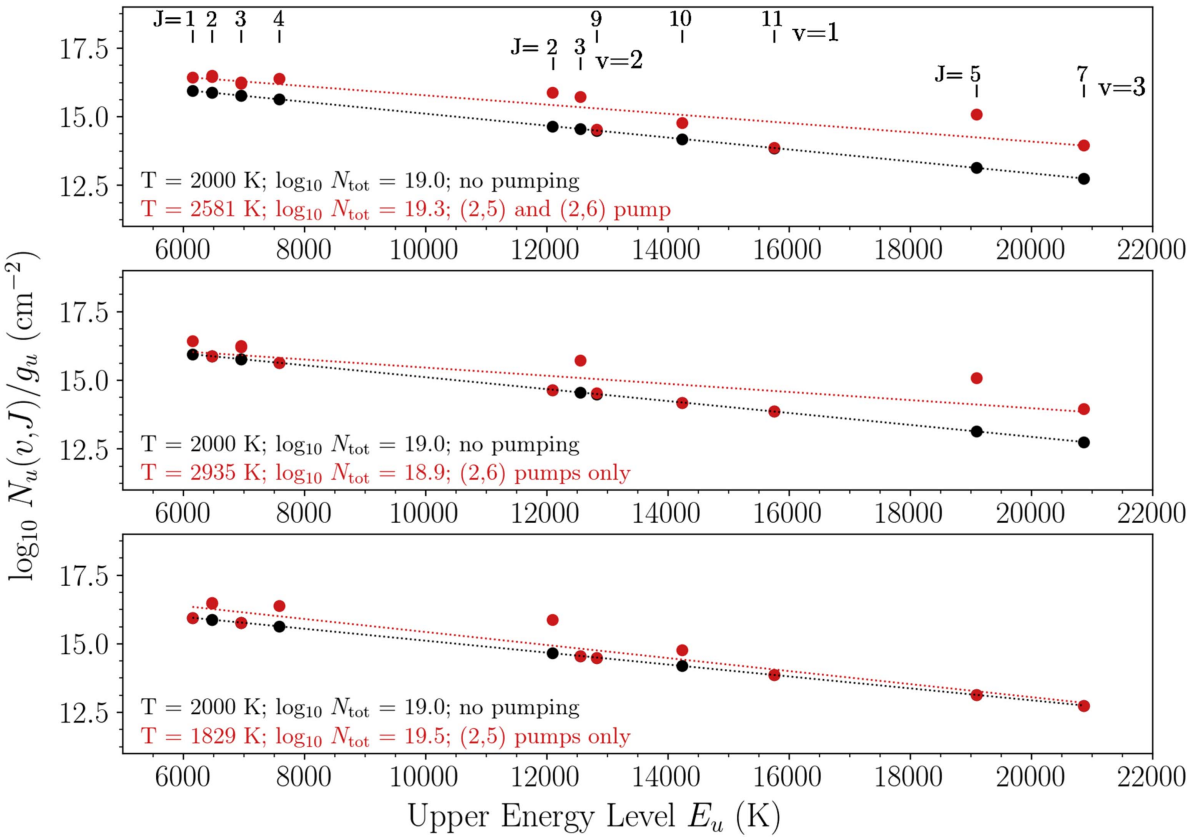

Figure 8. Example excitation diagrams using the 13 H_2 lines (Table 1) showing purely thermal populations in black ($N(H_2) = 10^{18}$ cm^{-2}, $T = 2000$ K, and ortho/para = 3), and excess population due to Lyα pumping from (v, J) = (2, 5) and (2, 6) in red. The dotted black and red lines show the fits to the black and red data points, respectively, and the black and red text in the lower-left corner of each subplot shows the fitted temperature and total H_2 column density corresponding to the color of the data points. Top: (2, 5) and (2, 6) both absorbed 0.05 erg cm^{-2} s^{-1} sr^{-1}, selected as an illustrative amount. Middle: (2, 5) absorbed no flux, and (2, 6) absorbed 0.05 erg cm^{-2} s^{-1} sr^{-1}. Bottom: (2, 5) absorbed 0.05 erg cm^{-2} s^{-1} sr^{-1}, and (2, 6) absorbed no flux.

for the region; Bally et al. 2015), we find a flux of 8.8×10^{-4} erg cm^{-2} s^{-1} sr^{-1}. As these two values are in good agreement, we assume 10^{-3} erg cm^{-2} s^{-1} sr^{-1} as the Lyα surface brightness passing through the shock.

We assume no self reversal and that the Lyα emission and H_2 absorption have velocity centroids of 0 km s^{-1}. For the H_2 population, we assume $T = 2000$ K, $N(H_2) = 10^{19}$ cm^{-2} and a Doppler broadening value $b = 5$ km s^{-1} (includes a turbulent velocity of 2 km s^{-1}). For a narrow profile (40 km s^{-1}), 4×10^{-4} erg cm^{-2} s^{-1} sr^{-1} is pumped into (1, 7) and no flux is pumped into (1, 4). For a broad profile (100 km s^{-1}), 1.7×10^{-4} erg cm^{-2} s^{-1} sr^{-1} is pumped into (1, 7), and 3.6×10^{-5} erg cm^{-2} s^{-1} sr^{-1} is pumped into (1, 4). In both cases, the Lyα enhancements in the near-IR lines are negligible and would not be detected by TripleSpec. The derived temperatures from the resulting excitation diagram are within 0.5% of the thermal population's temperature. Unless the Lyα surface brightness estimate is severely underestimated, Lyα pumping signatures from shocks should not be detectable in the near-IR. In the mid-IR, the 0–0 S(0), 0–0 S(1), and 0–0 S(2) show strong enhancements above their thermal flux values, but these lines should be subject to rapid re-thermalization due to collisional de-excitation with H atoms.

5.3. Nebular Lyα

We consider the possibility that resonant Lyα scattering from the bright H II region (M42) in the foreground could excite the H_2 fingers, akin to the planetary nebula scenario in Lupu et al. (2006). The source of the ionizing photons that create the H II region is the Trapezium cluster, and the brightest member, θ^1 Ori C, is the dominant driver of the H II region. The Trapezium cluster is approximately 0.25 pc in front of the ionization front separating the foreground H II region and the background OMC1 cloud core from which the BN/KL outflow emerges (Wen & O'Dell 1995; O'Dell 2001). Nebular Lyα, created from H I recombination, resonantly scatters around the nebula, impinging on the interface between the H II region and the molecular cloud. Any Lyα that escapes will be quickly attenuated over the sharp increase in density across the interface region and will not penetrate to most of the BN/KL outflow. However, some of the H_2 fingers have low extinction values and visibility at optical wavelengths indicate that they are poking through the ionization front (Graham et al. 2003).

We determine the average Lyα surface brightness of the nebula from Hα (6563 Å). From the VLT/MUSE Hα image of Weilbacher et al. (2015), we measure the mean Hα surface brightness across the nebula to be $F(H\alpha) = 4.31 \times 10^{-2}$ erg cm^{-2} s^{-1} sr^{-1}. Assuming Case A recombination as an upper limit, the flux ratio between Lyα and Hα $F(Ly\alpha)/F(H\alpha) \approx 11$ at $T = 10^4$ K (Hummer & Storey 1987). Thus, $F(Ly\alpha) = 0.47$ erg cm^{-2} s^{-1} sr^{-1}.

To determine the amount of dust and gas in the interface region separating the nebular Lyα photons and the H_2 fingers, we compare the Brγ/Paβ extinction map that measures the dust foreground with the nebula (described in Section 2) to the extinction map based on the flux ratio of H_2 1–0 Q(3) and

Table 3
Rovibrational H_2 Transitions Receiving $\geqslant$0.1% of Lyα Pumping Flux

Transition	λ_0 (Å)	E_u (K)	A_{ul} (10^{-7} s^{-1})	Lyα Cascade[a] (%)	Transition	λ_0 (Å)	E_u (K)	A_{ul} (10^{-7} s^{-1})	Lyα Cascade[a] (%)
0–0 S(8)	50376	8687	3.23	1.2	3–2 Q(2)	27186	17387	4.84	0.85
0–0 S(7)	55025	7201	2.0	0.20	3–2 Q(3)	27312	17817	4.42	3.6
0–0 S(6)	61041	5831	1.14	10.6	3–2 Q(4)	27481	18385	4.18	2.2
0–0 S(5)	69074	4586	0.59	3.3	3–2 Q(5)	27693	19085	3.99	2.3
0–0 S(4)	80241	3474	0.26	35.7	3–2 Q(6)	27948	19912	3.79	4.1
0–0 S(3)	96645	2503	0.1	18.4	3–2 Q(7)	28249	20857	3.58	0.22
0–0 S(2)	122784	1681	0.03	63.9	3–2 O(2)	29620	16952	14.1	0.11
0–0 S(1)	170346	1015	0.005	50.0	3–2 O(3)	31638	17097	6.87	2.2
0–0 S(0)	282184	509	0.0003	84.8	3–2 O(4)	33959	17387	4.87	0.86
1–1 S(8)	53100	14233	2.92	0.49	3–2 O(5)	36635	17817	3.52	2.9
1–1 S(6)	64315	11523	1.05	2.1	3–2 O(6)	39727	18385	2.53	1.3
1–1 S(5)	72764	10342	0.54	0.11	3–2 O(7)	43317	19085	1.79	1.1
1–1 S(4)	84511	9286	0.25	0.85	3–1 S(0)	12620	17387	3.19	0.56
1–1 S(3)	101769	8365	0.09	0.20	3–1 S(1)	12330	17817	4.68	3.8
1–0 S(8)	17124	14233	2.34	0.40	3–1 S(2)	12075	18385	5.76	3.0
1–0 S(6)	17874	11523	3.54	7.1	3–1 S(3)	11856	19085	6.59	3.9
1–0 S(5)	18355	10342	3.95	0.77	3–1 O(3)	14180	17097	4.99	1.6
1–0 S(4)	18918	9286	4.19	14.4	3–1 O(4)	14677	17387	2.86	0.50
1–0 S(3)	19575	8365	4.21	9.3	3–1 O(5)	15220	17817	1.98	1.6
1–0 S(2)	20337	7584	3.98	9.4	3–1 O(6)	15812	18385	1.38	0.72
1–0 S(1)	21218	6951	3.47	11.6	3–1 O(7)	16455	19085	0.96	0.56
1–0 S(0)	22232	6471	2.53	4.0	4–3 S(6)	21441	26622	2.3	0.48
1–0 Q(1)	24065	6148	4.29	9.1	4–3 S(5)	21997	25626	3.24	0.17
1–0 Q(2)	24134	6471	3.03	4.7	4–3 S(4)	22658	24735	4.04	2.0
1–0 Q(3)	24237	6951	2.78	9.3	4–3 S(3)	23435	23956	4.6	0.97
1–0 Q(4)	24374	7584	2.65	6.3	4–3 S(1)	25404	22761	4.51	1.6
1–0 Q(5)	24547	8365	2.55	5.6	4–3 S(0)	26631	22354	3.49	0.16
1–0 Q(6)	24754	9286	2.44	8.4	4–2 S(0)	13422	22354	5.25	0.23
1–0 Q(7)	24997	10342	2.34	0.46	4–2 S(1)	13113	22761	7.56	2.7
1–0 Q(8)	25276	11523	2.23	4.4	4–2 S(2)	12843	23296	9.15	2.8
1–0 Q(10)	25944	14233	1.99	0.34	4–2 S(3)	12613	23956	10.3	2.2
1–0 O(8)	41642	9286	0.74	2.5	4–2 O(3)	15094	22081	7.69	1.5
1–0 O(7)	38080	8365	1.06	2.3	4–2 O(4)	15631	22354	5.17	0.23
1–0 O(6)	35009	7584	1.5	3.5	4–2 O(5)	16219	22761	3.67	1.3
1–0 O(5)	32350	6951	2.08	6.9	4–2 O(6)	16862	23296	2.63	0.82
1–0 O(4)	30038	6471	2.9	4.5	4–2 O(7)	17562	23956	1.88	0.40
1–0 O(3)	28025	6148	4.22	9.0	4–2 O(8)	18323	24735	1.33	0.65
1–0 O(2)	26268	5986	8.54	2.3	4–2 O(10)	20058	26622	0.64	0.13
2–1 S(8)	18153	19449	2.43	0.18	5–3 Q(1)	14909	26747	11.6	1.2
2–1 S(6)	18938	16883	4.31	5.7	5–3 Q(3)	15036	27386	7.63	1.6
2–1 S(5)	19444	15764	5.06	0.74	5–3 Q(4)	15138	27889	7.36	1.3
2–1 S(2)	21541	13150	5.6	6.5	5–3 Q(5)	15267	28509	7.17	0.98
2–1 S(1)	22477	12549	4.98	7.4	5–3 Q(6)	15424	29240	7.0	2.0
2–1 S(0)	23556	12094	3.68	1.7	5–3 Q(7)	15608	30075	6.82	0.24
2–1 Q(1)	25509	11788	6.37	4.6	5–3 Q(8)	15821	31008	6.64	1.1
2–1 Q(2)	25585	12094	4.49	2.1	5–3 O(3)	16111	26747	11.1	1.2
2–1 Q(3)	25698	12549	4.12	6.2	5–3 O(5)	17333	27386	5.53	1.1
2–1 Q(4)	25849	13150	3.91	4.5	5–3 O(6)	18035	27889	4.05	0.74
2–1 Q(7)	26535	15764	3.41	0.50	5–3 O(7)	18803	28509	2.97	0.41
2–1 Q(8)	26843	16883	3.23	4.3	5–3 O(8)	19642	29240	2.16	0.61
2–1 Q(10)	27583	19449	2.84	0.20	6–4 S(1)	14958	31700	11.4	2.9
2–1 O(2)	27861	11635	3.47	0.20	6–4 S(2)	14658	32170	13.3	0.70
2–1 O(3)	29740	11788	6.39	4.7	6–4 S(3)	14405	32748	14.3	3.5
2–1 O(4)	31898	12094	4.4	2.1	6–4 Q(1)	15947	31103	14.0	0.59
2–1 O(5)	34379	12549	3.17	4.7	6–4 Q(3)	16095	31700	9.15	2.4
2–1 O(6)	37239	13150	2.28	2.6	6–4 Q(4)	16214	32170	8.79	0.47
2–0 S(5)	10849	15764	3.28	0.48	6–4 Q(5)	16364	32748	8.52	2.1
2–0 S(2)	11382	13150	2.38	2.8	6–4 Q(6)	16547	33430	8.27	2.1
2–0 S(1)	11622	12549	1.9	2.8	6–4 Q(7)	16762	34209	8.01	0.18
2–0 S(0)	11895	12094	1.27	0.60	6–4 Q(8)	17013	35078	7.73	2.5
2–0 Q(1)	12383	11788	1.61	1.2	6–4 O(3)	17246	31103	14.0	0.59
2–0 Q(2)	12419	12094	1.38	0.66	6–4 O(5)	18580	31700	7.23	1.9
2–0 Q(3)	12473	12549	1.29	1.9	6–4 O(6)	19352	32170	5.41	0.29

Table 3
(Continued)

Transition	λ_0 (Å)	E_u (K)	A_{ul} (10^{-7} s^{-1})	Lyα Cascade[a] (%)	Transition	λ_0 (Å)	E_u (K)	A_{ul} (10^{-7} s^{-1})	Lyα Cascade[a] (%)
2–0 Q(4)	12545	13150	1.25	1.4	6–4 O(7)	20200	32748	4.05	1.0
2–0 O(2)	12932	11635	12.8	0.73	7–5 O(5)	19983	35709	8.45	1.4
2–0 O(3)	13354	11788	1.94	1.4	7–5 O(7)	21780	36681	4.88	0.80
2–0 O(4)	13816	12094	1.03	0.49	7–5 Q(3)	17287	35709	9.8	1.6
2–0 O(5)	14321	12549	0.7	1.0	7–5 Q(5)	17606	36681	9.01	1.5
2–0 O(6)	14870	13150	0.47	0.55	7–5 Q(6)	17823	37312	8.68	2.5
3–2 S(6)	20119	21915	3.59	2.5	7–5 Q(8)	18381	38836	7.93	2.7
3–2 S(5)	20650	20857	4.53	0.27	7–5 S(1)	16055	35709	11.7	1.9
3–2 S(4)	21278	19912	5.25	5.7	7–5 S(3)	15479	36681	13.8	2.3
3–2 S(3)	22013	19085	5.65	3.3	7–5 S(4)	15268	37312	13.6	3.9
3–2 S(2)	22870	18385	5.65	2.9	7–5 S(6)	14993	38836	11.3	3.8
3–2 S(1)	23865	17817	5.15	4.2	8–6 O(5)	21568	39419	8.81	1.3
3–2 S(0)	25014	17387	3.89	0.69	8–6 S(1)	17301	39419	10.6	1.6
3–2 Q(1)	27102	17097	7.05	2.3	8–6 S(3)	16707	40311	11.7	1.8

Note. Upper-level energies (E_u) and wavelengths (λ_0) were calculated through Herzberg (1950). Einstein A coefficients (A_{ul}) are from Wolniewicz et al. (1998).
[a] As in Table 1, the Lyα cascade column denotes what percentage of the flux pumped from the (2, 5) and (2, 6) levels cascades through these lines. The ortho transitions' percentages are calculated by normalizing to the flux pumped out of (2, 5) and the para transitions' are calculated by normalizing to the flux pumped out of the (2, 6) level of the ground state.

1–0 S(1) from Youngblood et al. (2016), which measures the dust foreground to the nebula and the dust between the H_2 fingers and the nebula. By subtracting the two extinction maps, we measure the dust extinction between the Lyα photons and the BN/KL outflow, and find the lowest values to be $A_V \sim 0.5$–1 mag. Assuming $R_V = 5.5$, a typical value for star-forming regions in the Milky Way with large dust grains, and extinction curves presented in Draine (2011), $A_V = 1$ corresponds to $A_{Ly\alpha} = 1.4$. Therefore, the nebular Lyα is attenuated by at least 70% due to dust alone ($A_\lambda = 2.5 \log_{10}[F_\lambda^{emit}/F_\lambda^{obs}]$). Assuming no H_2, the column of H I gas associated with $E(B\text{–}V) = A_V/R_V = 0.182$ is $N(\mathrm{H\,I}) = 4.93 \times 10^{21} \times E(B\text{–}V)\,\mathrm{cm^{-2}\,mag^{-1}} = 9.0 \times 10^{20}\,\mathrm{cm^{-2}}$ (Diplas & Savage 1994). For this H I column density and Doppler broadening values $b \leqslant 100\,\mathrm{km\,s^{-1}}$, the optical depth of the Lyα line core is $10^6 \leqslant \tau_{Ly\alpha} \leqslant 10^8$ and the attenuation only becomes non-zero outside $\pm 500\,\mathrm{km\,s^{-1}}$. There are other H_2 electronic transitions within $\pm 1000\,\mathrm{km\,s^{-1}}$ of Lyα that could be pumped (e.g., Herczeg et al. 2006), but nebular Lyα emission would not be broad enough and/or Doppler shifted enough to overlap with these transitions.

5.4. Limitations of the Lyα Pumping Model

Our simple model neglects collisional de-excitation, or re-thermalization, of the level populations on timescales shorter than the radiative decay timescale. The critical density, where de-excitation due to collisions with H atoms is equal to the rate of radiative de-excitation, is $n(\mathrm{H\,I}) \sim 10^6\,\mathrm{cm^{-3}}$ for lines like 1–0 S(1), 1–0 S(2), and 2–1 S(1) at 2000 K (Le Bourlot et al. 1999). Bally et al. (2015) estimate that the densities of the H_2 bullets must be approximately 10^4 times greater than the medium through which they are traveling to have sustained their motion over large distances. The medium's density is 10^2–$10^3\,\mathrm{cm^{-3}}$, so the number density of the bullets is likely $n(H_2) \sim 10^7\,\mathrm{cm^{-3}}$. Assuming $n(\mathrm{H\,I})/n(H_2) \sim 10^{-1}$, which is in between the typical values for shocks associated with low-mass star formation and PDRs (Le Bourlot et al. 1999), n(H I) is approximately the critical density. However, this estimate assumes that the entire bullet mass is shocked, which is likely not the case. We provide a second estimate of the shocked gas density by assuming that the H_2 emission spreads uniformly across the typical width of an emitting H_2 knot ($4'' = 2.4 \times 10^{16}$ cm) and the path length is equal to the width. Assuming a large total H_2 column density ($N(H_2) = 10^{20}\,\mathrm{cm^{-2}}$), we find that $n(H_2) \sim 4000\,\mathrm{cm^{-3}}$ and therefore $n(\mathrm{H\,I}) \sim 400\,\mathrm{cm^{-3}}$, indicating that the observed near-IR transitions would not be significantly affected by collisional de-excitation. Based on the second density estimate, we conclude that observed near-IR transitions are only affected to a small degree by collisional de-excitation. However, lower (v, J) transitions will be significantly affected, such as the 0–0 rotational lines which show large excess flux signatures in the radiative cascade calculation (Table 3).

The excess flux calculation does not account for the potentially lower-than-thermal fluxes in quadrupole lines originating from the (2, 6) and (2, 5) states. Given the long lifetimes of the (2, 6) and (2, 5) states and the strength of the two Lyman band transitions pumping out of this state, we do not allow radiation in these levels to continue to cascade down to the ground state. If it is physically accurate that all of the H_2 molecules from the (2, 6) and (2, 5) levels should be immediately pumped, then the observed column densities in these levels should be very small, and lower (v, J) levels should also be affected.

6. Summary

Using the H_2 de-reddened integrated intensity maps from Youngblood et al. (2016), we have measured the H_2 temperature and column density on a spaxel-by-spaxel basis across the Orion BN/KL outflow. Most of the region is well characterized by single-temperature fits with $T(H_2) \sim 2000$–2500 K, with the H_2 fingers farthest from the outflow origin showing higher temperatures and lower column densities. This gas comprises 10^{-5}–10^{-3} of the total H_2 column density. We also show that our set of 13 H_2 lines from the near-IR H and K bands is not conducive to detecting multiple temperature components, and our

measured temperatures are subject to biases based on the range of the upper-level energies probed by the lines.

Comparing our column density results with the CO column density of $T = 2500$ K gas measured by *Herschel* (Goicoechea et al. 2015), we find $CO/H_2 = 2 \times 10^{-3}$, which is in significant excess of the canonical 2.7×10^{-4} value (Lacy et al. 1994). The CO column density was measured from lines near 100 μm, and the H_2 column density was measured near 2 μm, so dust extinction could explain this difference. Other possible effects on the observed CO/H_2 fractional abundance could be incorrect assumptions on co-spatiality of the CO and H_2, and an overestimation of the CO column density. If the true CO/H_2 abundance is in agreement with the canonical value, and only dust extinction is affecting our measurement of CO/H_2, then an extincting layer of $A_V = 17$ mag must lie behind the observed H_2, in addition to the foreground extinction of $A_V \sim 5$ mag. This would mean that we are only observing $\sim$10% of the $T = 2500$ K H_2 gas; the rest is completely obscured by dust.

We have also created a simple Lyα pumping model for warm H_2 populations, and we tabulate which near-IR and mid-IR lines should show evidence of excess flux due to fluorescence from Lyman band transitions. We find that in the presence of strong Lyα emission, fluorescence signatures are present in bright near-IR lines in the H and K bands, but we calculate that incident Lyα radiation is likely very small and would result in extremely weak fluorescence signatures. We do not detect Lyα fluorescence signatures in our excitation diagrams, and the 2000–2500 K temperatures of the region are consistent with shock heating.

We thank the referee for suggestions that improved the manuscript, and Jeremy Darling, Jason Glenn, Serena Criscuoli, and Mihály Horányi for thoughtful guidance on the methodology and analysis.

Facility: Apache Point Observatory (TripleSpec).

Software: Astropy (Robitaille et al. 2013), IPython (Perez & Granger 2007), Matplotlib (Hunter 2007), molecular-hydrogen (https://github.com/keflavich/molecular_hydrogen), NumPy and SciPy (van der Walt et al. 2011).

ORCID iDs

Allison Youngblood https://orcid.org/0000-0002-1176-3391
Kevin France https://orcid.org/0000-0002-1002-3674
Adam Ginsburg https://orcid.org/0000-0001-6431-9633
Keri Hoadley https://orcid.org/0000-0002-8636-3309
John Bally https://orcid.org/0000-0001-8135-6612

References

Abgrall, H., Roueff, E., & Drira, I. 2000, A&AS, 141, 297
Abgrall, H., Roueff, E., Launay, F., Roncin, J. Y., & Subtil, J. L. 1993, A&AS, 101, 273
Bally, J., Cunningham, N. J., Moeckel, N., et al. 2011, ApJ, 727, 113
Bally, J., Ginsburg, A., Arce, H., et al. 2017, ApJ, 837, 60
Bally, J., Ginsburg, A., Silvia, D., & Youngblood, A. 2015, A&A, 579, A130
Bally, J., & Zinnecker, H. 2005, AJ, 129, 2281
Beckwith, S., Persson, S. E., Neugebauer, G., & Becklin, E. E. 1978, ApJ, 223, 464
Bruderer, S. 2013, A&A, 559, A46
Bruderer, S., van Dishoeck, E. F., Doty, S. D., & Herczeg, G. J. 2012, A&A, 541, A91
Burgh, E. B., France, K., & McCandliss, S. R. 2007, ApJ, 658, 446
Burton, M. G., Minchin, N. R., Hough, J. H., et al. 1991, ApJ, 375, 611
Chatterjee, S., & Tan, J. C. 2012, ApJ, 754, 152
Colgan, S. W. J., Schultz, A. S. B., Kaufman, M. J., Erickson, E. F., & Hollenbach, D. J. 2007, ApJ, 671, 536
Cyganowski, C. J., Whitney, B. A., Holden, E., et al. 2008, AJ, 136, 2391
Dickman, R. L. 1978, ApJS, 37, 407
Diplas, A., & Savage, B. D. 1994, ApJ, 427, 274
Doi, T., O'Dell, C. R., & Hartigan, P. 2004, AJ, 127, 3456
Draine, B. T. 2011, Physics of the Interstellar and Intergalactic Medium (Princeton, NJ: Princeton Univ. Press)
Dzib, S. A., Loinard, L., Rodríguez, L. F., et al. 2017, ApJ, 834, 139
Eislöffel, J. 2000, A&A, 354, 236
France, K., Herczeg, G. J., McJunkin, M., & Penton, S. V. 2014, ApJ, 794, 160
France, K., Schindhelm, E., Herczeg, G. J., et al. 2012, ApJ, 756, 171
Geballe, T. R., Burton, M. G., & Pike, R. E. 2017, ApJ, 837, 83
Goddi, C., Humphreys, E. M. L., Greenhill, L. J., Chandler, C. J., & Matthews, L. D. 2011, ApJ, 728, 15
Goicoechea, J. R., Chavarría, L., Cernicharo, J., et al. 2015, ApJ, 799, 102
Gómez, L., Rodríguez, L. F., Loinard, L., et al. 2008, ApJ, 685, 333
Graham, M. F., Meaburn, J., & Redman, M. P. 2003, MNRAS, 343, 419
Gutermuth, R. A., Megeath, S. T., Muzerolle, J., et al. 2004, ApJS, 154, 374
Hartigan, P., Raymond, J., & Hartmann, L. 1987, ApJ, 316, 323
Herczeg, G. J., Linsky, J. L., Valenti, J. A., Johns Krull, C. M., & Wood, B. E. 2002, ApJ, 572, 310
Herczeg, G. J., Linsky, J. L., Walter, F. M., Gahm, G. F., & Johns Krull, C. M. 2006, ApJS, 165, 256
Herczeg, G. J., Wood, B. E., Linsky, J. L., Valenti, J. A., & Johns Krull, C. M. 2004, ApJ, 607, 369
Herzberg, G. 1950, Molecular Spectra and Molecular Structure, Vol. 1, Spectra of Diatomic Molecules (New York: D. Van Nostrand Company, Inc.)
Hoadley, K., France, K., Arulanantham, N., Loyd, R. O. P., & Kruczek, N. 2017, ApJ, 846, 6
Hummer, D. G., & Storey, P. J. 1987, MNRAS, 224, 801
Hunter, J. D. 2007, CS&E, 9, 90
Kasliwal, M. M., Bally, J., Masci, F., et al. 2017, ApJ, 839, 88
Kwan, J., & Scoville, N. 1976, ApJL, 210, L39
Lacy, J. H., Knacke, R., Geballe, T. R., & Tokunaga, A. T. 1994, ApJL, 428, L69
Lacy, J. H., Sneden, C., Kim, H., & Jaffe, D. T. 2017, ApJ, 838, 66
Le Bourlot, J., Pineau des Forets, G., & Flower, D. R. 1999, MNRAS, 305, 802
Le, H. A. N., Pak, S., Kaplan, K. F., et al. 2017, ApJ, 841, 13
Liu, W., & Dalgarno, A. 1996, ApJ, 467, 446
Luhman, K. L., Robberto, M., Tan, J. C., et al. 2017, ApJL, 838, 3
Lupu, R. E., France, K., & McCandliss, S. R. 2006, ApJ, 644, 981
Mathis, J. S. 1990, ARA&A, 28, 37
McJunkin, M., France, K., Schindhelm, E., et al. 2016, ApJ, 828, 69
Menten, K. M., Reid, M. J., Forbrich, J., & Brunthaler, A. 2007, A&A, 474, 515
O'Dell, C. R. 2001, ARA&A, 39, 99
Oh, H., Pyo, T.-S., Kaplan, K. F., et al. 2016, ApJ, 833, 275
Peng, T.-C., Zapata, L. A., Wyrowski, F., Güsten, R., & Menten, K. M. 2012, A&A, 544, L19
Perez, F., & Granger, B. E. 2007, CS&E, 9, 21
Pike, R. E., Geballe, T. R., Burton, M. G., & Chrysostomou, A. 2016, ApJ, 822, 82
Plambeck, R. L., & Wright, M. C. H. 2016, ApJ, 833, 219
Plambeck, R. L., Wright, M. C. H., Friedel, D. N., et al. 2009, ApJL, 704, L25
Robitaille, T. P., Tollerud, E. J., Greenfield, P., et al. 2013, A&A, 558, A33
Rodriguez, L. F., Dzib, S. A., Loinard, L., et al. 2017, ApJ, 834, 140
Rosenthal, D., Bertoldi, F., & Drapatz, S. 2000, A&A, 356, 705
Sahai, R., Claussen, M., Sánchez Contreras, C., Morris, M., & Sarkar, G. 2008, ApJ, 680, 483
Schindhelm, E., France, K., Herczeg, G. J., et al. 2012, ApJL, 756, L23
Schwartz, R. D. 1983, ApJL, 268, L37
Shull, J. M. 1978, ApJ, 219, 877
Smith, N., Whitney, B. A., Conti, P. S., De Pree, C. G., & Jackson, J. M. 2009, MNRAS, 399, 952
Snell, R. L., Scoville, N. Z., Sanders, D. B., & Erickson, N. R. 1984, ApJ, 284, 176
Sugai, H., Usuda, T., Kataza, H., et al. 1994, ApJ, 420, 746
Tan, J. C. 2004, ApJL, 607, L47
van der Walt, S., Colbert, S. C., & Varoquaux, G. 2011, CS&E, 13, 22
van Dishoeck, E. F., & Black, J. H. 1988, ApJ, 334, 771
Visser, R., van Dishoeck, E. F., & Black, J. H. 2009, A&A, 503, 323
Walter, F. M., Herczeg, G., Brown, A., et al. 2003, AJ, 126, 3076

Watson, D. M., Genzel, R., Townes, C. H., & Storey, J. W. V. 1985, ApJ, 298, 316
Weilbacher, P. M., Monreal-Ibero, A., Kollatschny, W., et al. 2015, A&A, 582, A114
Wen, Z., & O'Dell, C. R. 1995, ApJ, 438, 784
Wilson, T. L., Serabyn, E., Henkel, C., & Walmsley, C. M. 1986, A&A, 158, L1
Wolfire, M. G., & Konigl, A. 1991, ApJ, 383, 205
Wolniewicz, L., Simbotin, I., & Dalgarno, A. 1998, ApJS, 115, 293
Wolven, B. C., Feldman, P. D., Strobel, D. F., & McGrath, M. A. 1997, ApJ, 475, 835
Youngblood, A., Ginsburg, A., & Bally, J. 2016, AJ, 151, 173
Zapata, L. A., Schmid-Burgk, J., Ho, P. T. P., Rodríguez, L. F., & Menten, K. M. 2009, ApJL, 704, L45
Zapata, L. A., Schmid-Burgk, J., Pérez-Goytia, N., et al. 2013, ApJL, 765, L29